In-situ transformed Mott-Schottky heterointerface in silver/manganese oxide nanorods boosting oxygen reduction, oxygen evolution, and hydrogen evolution reactions

Ruiqi Cheng[1], Kaiqi Li[2], Huanxin Li[3], Fengzhan Sun[4], Xiaoqian He[4], Tianshuo Zhao[1], Jiao Zhang[1,*] and Chaopeng Fu[1,*]

[1] Shanghai Key Laboratory of Advanced High-temperature Materials and Precision Forming, School of Materials Science and Engineering, Shanghai Jiao Tong University, Shanghai 200240, P. R. China

[2] Christopher Ingold Laboratory, Department of Chemistry, University College London, London WC1H 0AJ, UK

[3] Department of Chemistry, Physical & Theoretical Chemistry Laboratory, University of Oxford, South Parks Road, Oxford OX1 3QZ, UK

[4] Center of Hydrogen Science, School of Materials Science and Engineering, Shanghai Jiao Tong University, Shanghai 200240, P. R. China

*Corresponding authors:

zj119@sjtu.edu.cn (Prof. Jiao Zhang)

chaopengfu@sjtu.edu.cn (Prof. Chaopeng Fu)

ABSTRACT

The development of non-platinum group metal (non-PGM) and efficient multifunctional electrocatalysts for oxygen reduction reaction (ORR), oxygen evolution reaction (OER), and hydrogen evolution reaction (HER) with high activity and stability remains a great challenge. Herein, by in-situ transforming silver manganese composite oxide heterointerface into boosted Mott-Schottky heterointerface through a facile carbon reduction strategy, a nanorod-like silver/manganese oxide with superior multifunctional catalytic activities for ORR, OER and HER and stability was obtained. The nanorod-like silver/manganese oxide with Mott-Schottky heterointerface (designated as Ag/Mn_3O_4) exhibits an ORR half-wave potential of 0.831 V (vs. RHE) in 0.1 M KOH, an OER overpotential of 338 mV and an HER overpotential of 177 mV at the current density of 10 mA cm^{-2} in 1 M KOH, contributing to its noble-metal benchmarks comparable performance in aqueous aluminum-air (Al-air) battery and laboratorial overall water splitting electrolytic cell. Moreover, in-situ electrochemical Raman and synchrotron radiation spectroscopic measurements were conducted to further illustrate the catalytic mechanism of Ag/Mn_3O_4 Mott-Schottky heterointerface towards various electrocatalytic reactions. At the heterointerface, the Ag phase serves as the electron donor and the active phase for ORR and HER, while the Mn_3O_4 phase serves as the electron acceptor and the active phase for OER, respectively. This work deepens the understanding of the Mott-Schottky effect on electrocatalysis and fills in the gap in fundamental physical principles that are behind measured electrocatalytic activity,

which offers substantial implications for the rational design of cost-effective multifunctional electrocatalysts with Mott-Schottky effect.

KEYWORDS

Heterointerface; Electron donor-acceptor pair; Electrocatalyst; Al-air battery; Water splitting

1 Introduction

Developing renewable green energy conversion technologies to reduce the reliance on carbon-based energy resources has been a widely studied research topic for decades [1]. Among them, fuel cells, metal-air batteries, and electrochemical water splitting electrolyzers are considered as promising devices for efficiently utilizing clean energy [2, 3]. However, the sluggish kinetics of oxygen reduction reaction (ORR), oxygen evolution reaction (OER), and hydrogen evolution reaction (HER) greatly limit their practical applications [4, 5]. Platinum group metal (PGM) materials are currently well-known effective electrocatalysts. However, the low stability and scarcity of PGMs significantly hinder their large-scale production [6, 7]. Therefore, it is urgent to develop low-cost and highly efficient non-PGM electrocatalyst alternatives. Earth-abundant transition metal oxides have been widely investigated as substitutes for PGM materials for these electrocatalytic reactions [8, 9]. However, typical transition metal oxides possess low conductivities and activities, which can be improved by constructing heterointerfaces with other different phases. This rationally designed heterointerface between two different phases plays a key role in determining

the activities of electrocatalysts. The benefits brought by heterointerfaces can be divided into two types: (1) Heterointerface with modulated electronic structure can regulate the adsorption energy of different electrocatalytic reaction intermediates and enable them more easily be transformed into the ultimate product, resulting in enhanced activities for electrocatalytic reactions [10-12]; (2) The formation of heterointerface can construct a unique built-in electric field, as a fast electron pathway, contributing to the increased charge transfer and leading to more electrons participating in catalytic reactions at the heterointerface [13-15]. Generally, heterointerface between two metal oxides is considered as oxide heterointerface, and such a heterointerface with optimized electronic structure can promote the electrocatalytic performance through directly serving as active sites [12]. However, due to the similar energy bands of different semiconducting metal oxides, the variation degree of the electronic structure by forming oxide heterointerface is limited [16]. Furthermore, heterointerfaces can also be formed by compounding metals to metal oxides to create Mott-Schottky heterointerface [17, 18]. The large Mott-Schottky barrier between metal and metal oxide in the heterointerface is able to exhibit Mott-Schottky effect, which can more efficiently modulate the electric field to accelerate electron transfer during electrocatalytic reactions [19, 20]. The function mechanism of Mott-Schottky heterointerface is that the electrons will flow spontaneously from the metal side to the semiconductor side until the work functions on both sides are equal and Fermi energy levels achieve equilibrium [21]. During this process, a fast electron pathway is constructed for electrons participating in

electrocatalytic reactions [19]. These benefits clearly explain the optimized electronic and energy band structure of Mott-Schottky heterointerface with high intrinsic catalytic activity [22, 23]. Therefore, designing Mott-Schottky heterointerface is a promising strategy for boosting the catalytic activity of metal oxide-based electrocatalysts. However, the structure-activity relationship between the heterointerface with Mott-Schottky effect and electrocatalytic activity is still ambiguous.

In this work, a multi-functional electrocatalyst with Ag/Mn_3O_4 Mott-Schottky heterointerface is presented by compounding earth-abundant manganese oxide with silver. Firstly, silver and manganese oxide with oxide heterointerface ($Ag_2Mn_8O_{16}/MnO_2$) was obtained through a facile hydrothermal synthesis. Then, the $Ag_2Mn_8O_{16}/MnO_2$ was in-situ transformed to Ag/Mn_3O_4 Mott-Schottky heterointerface through carbon reduction. The Ag/Mn_3O_4 exhibits a more positive valence band and lower energy band gap compared with $Ag_2Mn_8O_{16}/MnO_2$ due to the existence of a large Mott-Schottky barrier between metallic Ag and semiconductive Mn_3O_4, which is favorable for electron transfer and participation in catalytic reactions. Moreover, various electrocatalysts with different heterointerfaces were studied for ORR, OER, and HER in alkaline electrolytes, and the results reveal that the Ag/Mn_3O_4 displays better electrocatalytic performance than $Ag_2Mn_8O_{16}/MnO_2$ because of the in-situ transformed Mott-Schottky heterointerface. Furthermore, the catalytic mechanisms of ORR, OER, and HER on the Ag/Mn_3O_4 Mott-Schottky heterointerface are discussed through in-situ electrochemical Raman and synchrotron

radiation spectroscopic studies. Additionally, the aluminum-air battery with Ag/Mn_3O_4 outputs a competitive power density to that with Pt/C, and the Ag/Mn_3O_4 also demonstrates comparable performance to RuO_2||Pt/C reference group when used as both anode and cathode in a laboratorial overall water splitting electrolytic cell.

2 Results and discussions

The Ag/Mn_3O_4 with Mott-Schottky heterointerface was prepared through a hydrothermal strategy following carbon reduction, as illustrated in Fig. S1. The $Ag_2Mn_8O_{16}/MnO_2$ was firstly hydrothermally prepared, and then the $Ag_2Mn_8O_{16}/MnO_2$ was reduced by carbon through thermal treatment to obtain the Ag/Mn_3O_4 final product. The oxide heterointerface between $Ag_2Mn_8O_{16}$ and MnO_2 was in-situ transformed into a Mott-Schottky heterointerface between Ag and Mn_3O_4 through carbon reduction (Fig. 1(a)). Moreover, X-ray diffraction (XRD) patterns in Fig. 1(b) show that the peaks in $Ag_2Mn_8O_{16}/MnO_2$ are ascribed to MnO_2 (PDF#72-1982) and $Ag_2Mn_8O_{16}$ (PDF#29-1143), and the peaks of Ag/Mn_3O_4 are assigned to Mn_3O_4 (PDF#80-0382) and Ag (PDF#87-0597). Particularly, the amount of carbon plays a key role in producing the Ag and Mn_3O_4 phases with Mott-Schottky heterointerface. When the amount of carbon was insufficient (e.g. 20 wt%), the obtained sample consists of Ag, Mn_3O_4, and MnO_2 (denoted as Ag/Mn_3O_4-MnO_2), which is confirmed by the XRD pattern in Fig. S2. This reveals that the MnO_2 phase in $Ag_2Mn_8O_{16}/MnO_2$ was not completely reduced. It is explained that $Ag_2Mn_8O_{16}$ was firstly decomposed into Ag and MnO_2, and the remaining MnO_2 was further reduced

by carbon black and transformed into Mn_3O_4 during thermal treatment, implying the $Ag_2Mn_8O_{16}/MnO_2$ heterointerface was transformed into Ag/Mn_3O_4 heterointerface. Scanning electron microscopy (SEM) reveals that $Ag_2Mn_8O_{16}/MnO_2$, Ag/Mn_3O_4-MnO_2, and Ag/Mn_3O_4 exhibit nanorod-like shape, and these nanorods are uniformly distributed (Fig. 1(c) and Fig. S3). Transmission electron microscopy (TEM) images confirm the nanorod structure of $Ag_2Mn_8O_{16}/MnO_2$ and Ag/Mn_3O_4 samples with a diameter of ~ 50 nm (Fig. 1(d) and Fig. S4). Moreover, the element mappings confirm the uniform distributions of Ag, Mn, and O elements in both $Ag_2Mn_8O_{16}/MnO_2$ and Ag/Mn_3O_4 (Fig. S5, Fig. S6 and Fig. 1(e-h)). These results suggest that both the morphological structure and element distribution of silver/manganese oxide nanorods can be finely retained after carbon reduction.

The heterointerfaces in $Ag_2Mn_8O_{16}/MnO_2$ and Ag/Mn_3O_4 were observed through high-resolution transmission electron microscopy (HRTEM). Fig. S7 displays the different layers in the $Ag_2Mn_8O_{16}/MnO_2$ nanorod, and the linear scan measurement manifests that the intensity peak of Mn corresponds to the intensity trough of Ag. This result clearly suggests that the area with an intensity peak of Mn is the MnO_2 phase and the area with an intensity peak of Ag is the $Ag_2Mn_8O_{16}$ phase. Moreover, the $Ag_2Mn_8O_{16}/MnO_2$ oxide heterointerface is further confirmed by the calculated crystal plane spacing and corresponding Fast Fourier Transform (FFT) patterns of two adjacent layers (Fig. S8). Similarly, the heterointerface in Ag/Mn_3O_4 is also clearly observed in the magnified HRTEM image (Fig. 1(i, j)), and the crystal plane spacing of the phase in the upper area is 0.235 nm, corresponding to the (111) plane of Ag

with hexagonal array distribution in face-centered cubic (fcc) structure (marked with red hexagon frame), while the crystal plane spacing of the phase in the lower area is 0.249 nm, corresponding to the (211) plane of Mn_3O_4 (Fig. 1(k, l)). The corresponding FFT patterns of both regions also indicate different crystal structures and electron densities of the Ag and Mn_3O_4 phases. These results clearly demonstrate the in-situ transformation of $Ag_2Mn_8O_{16}/MnO_2$ oxide heterointerface to Ag/Mn_3O_4 Mott-Schottky heterointerface.

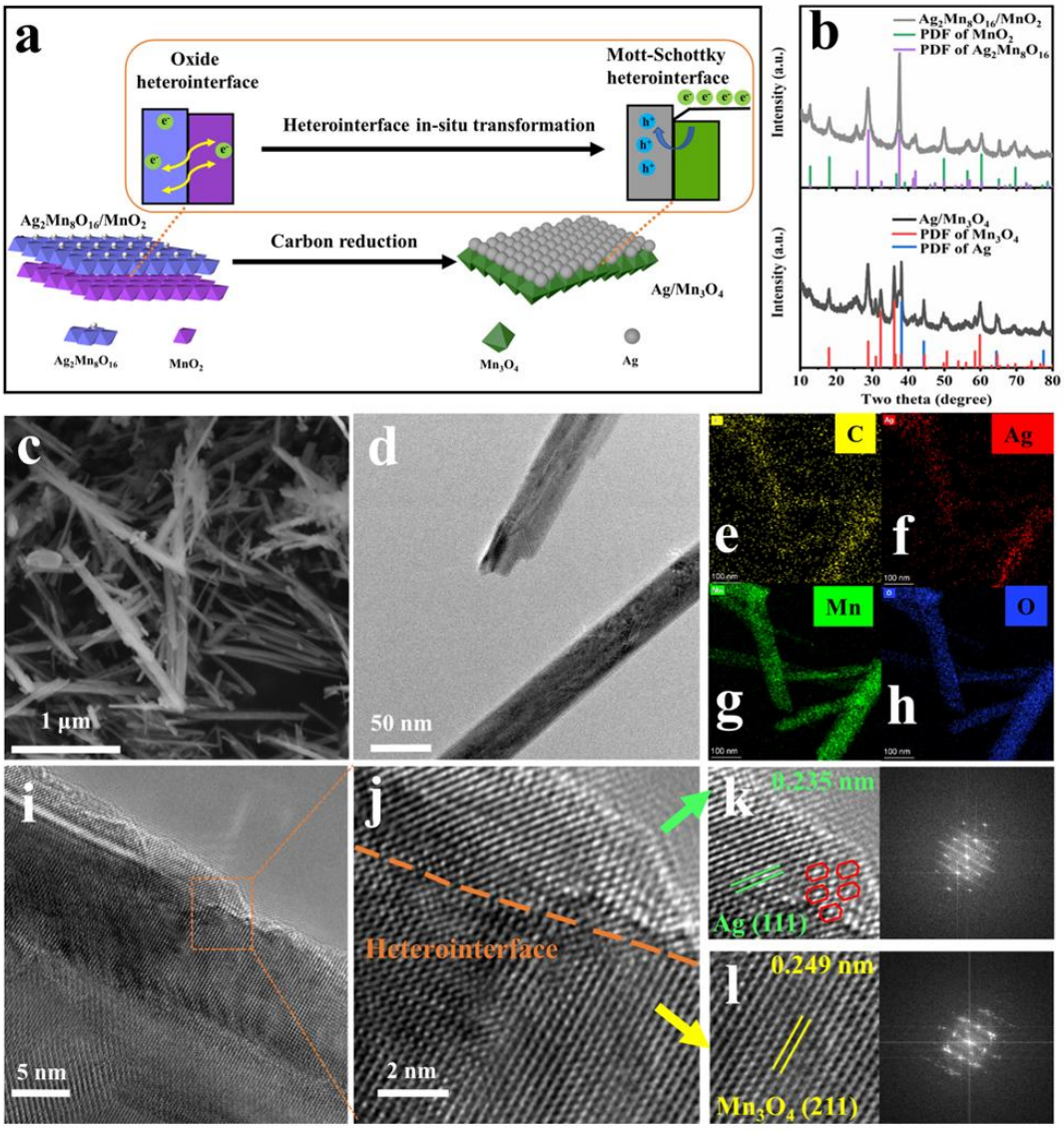

Figure 1 (a) Schematic illustration of the in-situ transformation of $Ag_2Mn_8O_{16}/MnO_2$ oxide heterointerface to Ag/Mn_3O_4 Mott-Schottky heterointerface. (b) XRD patterns of Ag/Mn_3O_4 and $Ag_2Mn_8O_{16}/MnO_2$. (c) SEM image, (d) TEM image, (e-h) Element mappings of C, Ag, Mn, and O, and (i) HRTEM image of Ag/Mn_3O_4. (j) HRTEM image of heterointerface between Ag and Mn_3O_4 in Ag/Mn_3O_4. (k, l) Lattice spacing calculations with corresponding FFT results of Mn_3O_4 and Ag phases in Ag/Mn_3O_4.

X-ray photoelectron spectroscopy (XPS) surveys reveal the presences of Ag, Mn, and O in all samples (Fig. S9). The deconvoluted Ag 3d spectra show that the doublet of $Ag_2Mn_8O_{16}/MnO_2$ at 367.9 and 373.9 eV are attributed to Ag (+1), and the formation of Ag (0) is confirmed by the doublet of Ag/Mn_3O_4 at 368.2 eV and 374.2 eV (Fig. 2(a)) [24]. Fig. 2(b) is the deconvoluted Mn 2p spectra of $Ag_2Mn_8O_{16}/MnO_2$ and Ag/Mn_3O_4. For the deconvoluted Mn 2p spectrum of $Ag_2Mn_8O_{16}/MnO_2$, the binding energies of Mn $2p_{3/2}$ peak at 643.4, 642.2, and 641.1 eV and those of Mn $2p_{1/2}$ peak at 654.9, 653.7, and 652.6 eV are ascribed to Mn^{IV}, Mn^{III}, and Mn^{II}, respectively [25, 26]. For the deconvoluted Mn 2p spectrum of Ag/Mn_3O_4, the Mn $2p_{3/2}$ and Mn $2p_{1/2}$ peaks for Mn^{IV} disappear, which is due to the reduction of MnO_2 into Mn_3O_4 [27]. The O 1s spectra of Ag/Mn_3O_4 and $Ag_2Mn_8O_{16}/MnO_2$ were deconvoluted into three peaks at 533.4 eV, 531.9 eV, and 530.1 eV, which can be ascribed to surface oxygen (O_{sur}), adsorbed oxygen (O_{ads}) and lattice oxygen (O_L), respectively (Fig. 2(c)) [28]. The ratio of $(O_{sur}+ O_{ads})/O_L$ represents the content of unsaturated oxygen species in the composite [29]. Here, after the $Ag_2Mn_8O_{16}/MnO_2$

was in-situ transformed into Ag/Mn_3O_4, the $(O_{sur}+O_{ads})/O_L$ ratio increased from 1.04 to 2.47, confirming the existence of less bonded lattice oxygen and more Mn atoms with lower coordination in Ag/Mn_3O_4 [30].

To analyze the energy band structure of Ag/Mn_3O_4 and $Ag_2Mn_8O_{16}/MnO_2$ heterointerfaces, ultraviolet photoelectron spectra (UPS) in Fig. 2(d) and Fig. 2(e) were used to determine their valence band maxima (E_{VBM}), cut-off edge (E_{cutoff}), and work function (Φ) was calculated according to the photoelectric law ($\Phi = 21.22$ eV $-$ ($E_{cutoff} - E_F$), here E_F is the Fermi energy level) [23]. To rule out the electric effect of unreacted mechanical mixed carbon black in Ag/Mn_3O_4 when comparing the band structure of various heterointerfaces, $Ag_2Mn_8O_{16}/MnO_2$@C was used as counterpart here. The work function of Ag/Mn_3O_4 is 4.55 eV, which is lower than that of $Ag_2Mn_8O_{16}/MnO_2$@C (4.61 eV). This can be attributed to the formation of the metallic Ag phase with a lower work function after carbon reduction. Unlike semiconductive manganese oxide with low electron mobility [31, 32], metallic Ag can release more electrons and these electrons will flow pass through the heterointerface and enter into the Mn_3O_4 phase to enable the Fermi energy levels of both sides equal (Fig. 2(f)) [33], leaving holes in the original Ag phase simultaneously. The Mott-Schottky barrier between them can induce electron redistribution to allow large amounts of electrons to pass the heterointerface spontaneously to not only maintain the balance of work function but also provide an efficient pathway for electron transfer, which greatly facilitates the catalytic process [19, 33, 34]. This phenomenon suggests that the Ag/Mn_3O_4 Mott-Schottky heterointerface contains massive electron

donor-acceptor pairs with Ag electron donors and Mn_3O_4 electron acceptors. The measured E_{VBM} of Ag/Mn_3O_4 and $Ag_2Mn_8O_{16}/MnO_2$ heterointerfaces are 0.71 and 0.36 eV, and the calculated valence bands (E_v) are 0.86 and 0.57 V (vs NHE), respectively [35]. Moreover, ultraviolet-visible spectroscopy (UV-vis) was used to determine the indirect band gaps of $Ag_2Mn_8O_{16}/MnO_2$ and Ag/Mn_3O_4 heterointerfaces. The band gaps (E_g) of $Ag_2Mn_8O_{16}/MnO_2$@C and Ag/Mn_3O_4 are 1.35 and 1.28 eV (Fig. S10). The energy band diagrams of $Ag_2Mn_8O_{16}/MnO_2$ and Ag/Mn_3O_4 heterointerfaces are depicted in Fig. 2(g). The positive shift of E_v after carbon reduction of $Ag_2Mn_8O_{16}/MnO_2$ indicates that more electrons have the potential to be involved in the catalytic reactions [36, 37]. In addition, the narrowed band gap of the Ag/Mn_3O_4 heterointerface can significantly improve the conductivity of the composite, which is also beneficial for the charge transfer during electrocatalytic reactions [38].

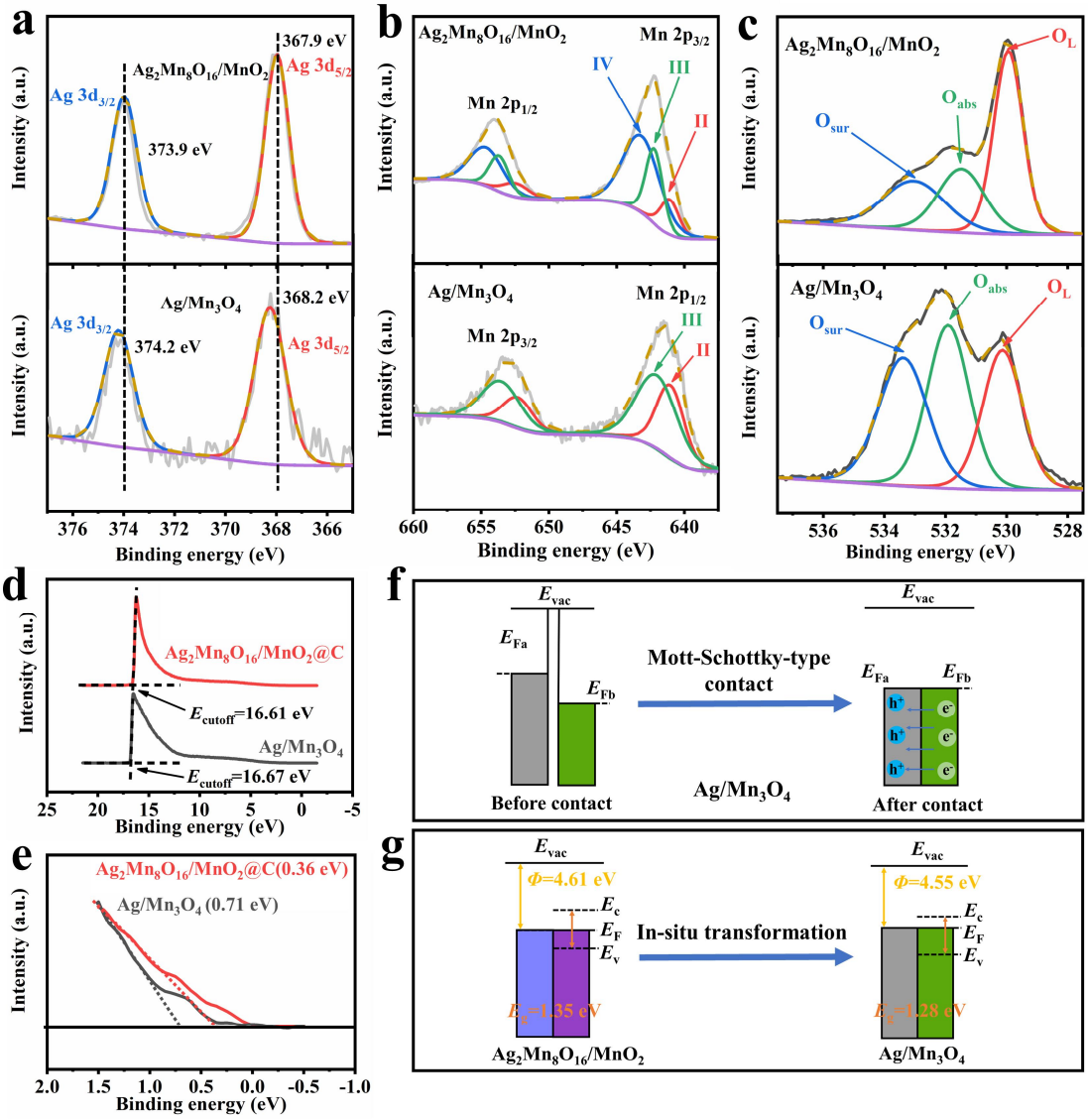

Figure 2 Deconvoluted (a) Ag 3d, (b) Mn 2p and (c) O 1s peaks of Ag/Mn_3O_4 and $Ag_2Mn_8O_{16}/MnO_2$. (d, e) UPS spectra of Ag/Mn_3O_4 and $Ag_2Mn_8O_{16}/MnO_2$@C. (f) The Mott-Schottky-type contact of Ag/Mn_3O_4 heterointerface. (g) Energy band diagrams of Ag/Mn_3O_4 and $Ag_2Mn_8O_{16}/MnO_2$ heterointerfaces.

The ORR electrocatalytic performances of Ag/Mn_3O_4, Ag/Mn_3O_4-MnO_2, and $Ag_2Mn_8O_{16}/MnO_2$ were measured in a 0.1 M KOH electrolyte. Cyclic voltammetry (CV) curves of Ag/Mn_3O_4, Ag/Mn_3O_4-MnO_2, and $Ag_2Mn_8O_{16}/MnO_2$ show clear

reduction peaks at 0.829 V, 0.816 V, and 0.805 V (Fig. S11), identifying the ORR catalytic activities of these samples. The Ag/Mn_3O_4 exhibits the most positive peak potential, suggesting the oxygen reduction on Ag/Mn_3O_4 is the most thermodynamic favorable [7]. Linear sweep voltammetry (LSV) curves of these samples in Fig. 3(a) show that the Ag/Mn_3O_4 possesses the most positive onset potential (E_{onset} = 0.942 V vs. RHE) and half-wave potential ($E_{1/2}$ = 0.831 V vs. RHE), revealing the highest ORR activity of the Ag/Mn_3O_4 (Table S1). Meanwhile, the ORR electrocatalytic activity of Ag/Mn_3O_4 is also comparable to that of commercial Pt/C electrocatalyst [39, 40]. Furthermore, the effect of molar ratio of Ag to Mn_3O_4 in Ag/Mn_3O_4 on the electrochemical activity was discussed. As shown in Fig. S12, the extracted $E_{1/2}$ of Ag/Mn_3O_4 is more positive than those of Ag/Mn_3O_4-1 and Ag/Mn_3O_4-2 (details of the synthesis see supporting information), suggesting that the optimized molar ratio of Ag to Mn_3O_4 in Ag/Mn_3O_4 contributes to the highest ORR activity. To prove the effect of Ag/Mn_3O_4 Mott-Schottky heterointerface, the catalytic performance of the mechanically mixed counterpart (denoted as Ag@Mn_3O_4) was also evaluated. LSV curves of Ag/Mn_3O_4 and Ag@Mn_3O_4 in Fig. 3(b) show that the Ag/Mn_3O_4 has more positive E_{onset} and $E_{1/2}$ than the Ag@Mn_3O_4, indicating the Ag/Mn_3O_4 heterointerface plays a key role in benefiting the ORR catalytic activity. Moreover, E_{onset} and $E_{1/2}$ of other silver/manganese oxide composite ORR electrocatalysts in recent literature are listed in Table S2 for comparison, and the E_{onset} and $E_{1/2}$ of Ag/Mn_3O_4 are competitive among them. Fig. 3(c) exhibits the corresponding Tafel slopes, all samples possess Tafel slopes lower than 120 mV dec^{-1}, suggesting that their ORR kinetics are mainly

determined by electron transfer and independent of the surface coverage of reaction intermediates [41]. The Ag/Mn_3O_4 possesses the lowest Tafel slope (90.2 mV dec^{-1}) among all samples including commercial Pt/C (96.1 mV dec^{-1}), manifesting the fastest kinetic process results from the Ag/Mn_3O_4 heterointerface with Mott-Schottky effect [42]. LSV curves with different rotating speeds and the corresponding fitted Koutecky-Levich (K-L) curves reveal the electron transfer numbers (n) of Ag/Mn_3O_4, Ag/Mn_3O_4-MnO_2, and $Ag_2Mn_8O_{16}/MnO_2$ are 3.98, 3.82, and 3.84, respectively (Fig. S13 and S14). Subsequently, the calculated kinetic current densities (J_k) of Ag/Mn_3O_4, Ag/Mn_3O_4-MnO_2, and $Ag_2Mn_8O_{16}/MnO_2$ through fitted K-L curves at the strong polarization region are 4.92, 4.42 and 3.36 mA cm^{-1}, respectively (Fig. S15), the Ag/Mn_3O_4 possesses the highest n and J_k, which means it has the highest intrinsic activity and an efficient four-electron pathway for ORR [43]. Moreover, double-layer capacitances (C_{dl}) of Ag/Mn_3O_4, Ag/Mn_3O_4-MnO_2, and $Ag_2Mn_8O_{16}/MnO_2$ were also calculated as 16.43, 14.02, and 12.71 μF cm^{-2}, respectively (Fig. S16 and S17). The largest C_{dl} of Ag/Mn_3O_4 demonstrates its most exposed active sites (Fig. 3(d)). This is because the Mott-Schottky heterointerface can provide more active sites due to the huge structural differences between the two different phases [37]. The rotating ring disk electrode (RRDE) measurement was conducted to calculate the n and the content of the byproduct HO_2^- during ORR. The disk and ring current densities of Ag/Mn_3O_4, Ag/Mn_3O_4-MnO_2, and $Ag_2Mn_8O_{16}/MnO_2$ are provided in Fig. S18. The byproduct (HO_2^-) yields of Ag/Mn_3O_4 is ~ 6% (Fig. 3(e)), again confirming the ORR on Ag/Mn_3O_4 mainly follows an efficient four-electron pathway. Additionally, through

fitting the electrochemical impedance spectroscopy (EIS) curves through the equivalent circuit provided in Fig. S19, the charge-transfer resistance (R_{ct}) of Ag/Mn_3O_4, Ag/Mn_3O_4-MnO_2, and $Ag_2Mn_8O_{16}/MnO_2$ can be calculated as 8.4, 14.7 and 118.4 ohm (Fig. S20). This result manifests the high efficiency of Ag/Mn_3O_4 heterointerface for electron transport.

LSV curves before and after 2000 cycles were used to evaluate the durability of Ag/Mn_3O_4 and Pt/C. As shown in Fig. 3(f), the Ag/Mn_3O_4 shows a slight shift of half-wave potential (~ 4 mV) after 2000 cycles, revealing good durability. Moreover, this half-wave potential shift is smaller than that of Pt/C (~ 9 mV) (Fig. S21), indicating better stability of Ag/Mn_3O_4 compared with PGM commercial counterpart. To further evaluate the stability of Ag/Mn_3O_4, the chronoamperometric curves performed at a constant potential of 0.81 V vs. RHE demonstrate that the current remains 89.3% of its initial value after 7.5 hrs, while the commercial Pt/C can only remain 77.8% of its initial value (Fig. S22), also suggesting the better durability of Ag/Mn_3O_4 compared with PGM benchmark. Furthermore, the heterointerface between Ag and Mn_3O_4 can still be maintained after the chronoamperometric test (Fig. S23), indicating the superior electrochemical stability of Ag/Mn_3O_4 originated from the structural robustness of the Mott-Schottky heterointerface in alkaline electrolyte. This is mostly ascribed to the fast electron pathway constructed by the Mott-Schottky heterointerface with high intrinsic activity.

To exhibit the practical application of Ag/Mn_3O_4, an aqueous alkaline Al-air battery based on Ag/Mn_3O_4 was assembled. In Fig. 3(g), the Al-air battery with Ag/Mn_3O_4

maintains plateaus of 1.59 V at 20 mA cm^{-2} and 1.09 V at 100 mA cm^{-2}, which is also comparable to Pt/C (1.59 V at 20 mA cm^{-2} and 1.18 V at 100 mA cm^{-2}). Fig. 3(h) is the current-voltage curves and corresponding power density curves of the Al-air battery with Ag/Mn_3O_4 and Pt/C cathode. The Al-air battery with Ag/Mn_3O_4 exhibits a maximum power density of 148.3 mW cm^{-2}, which is close to that of the Al-air battery with Pt/C (150.1 mW cm^{-2}). Moreover, the Al-air battery can be charged by refilling a new Al alloy anode in the electrolyte after 0.5 hrs' discharging, the voltage plateau can be maintained at 1.56 V after mechanical discharging for three times (Fig. 3(i)), indicating the superior stability of Ag/Mn_3O_4 during long-term practical discharging.

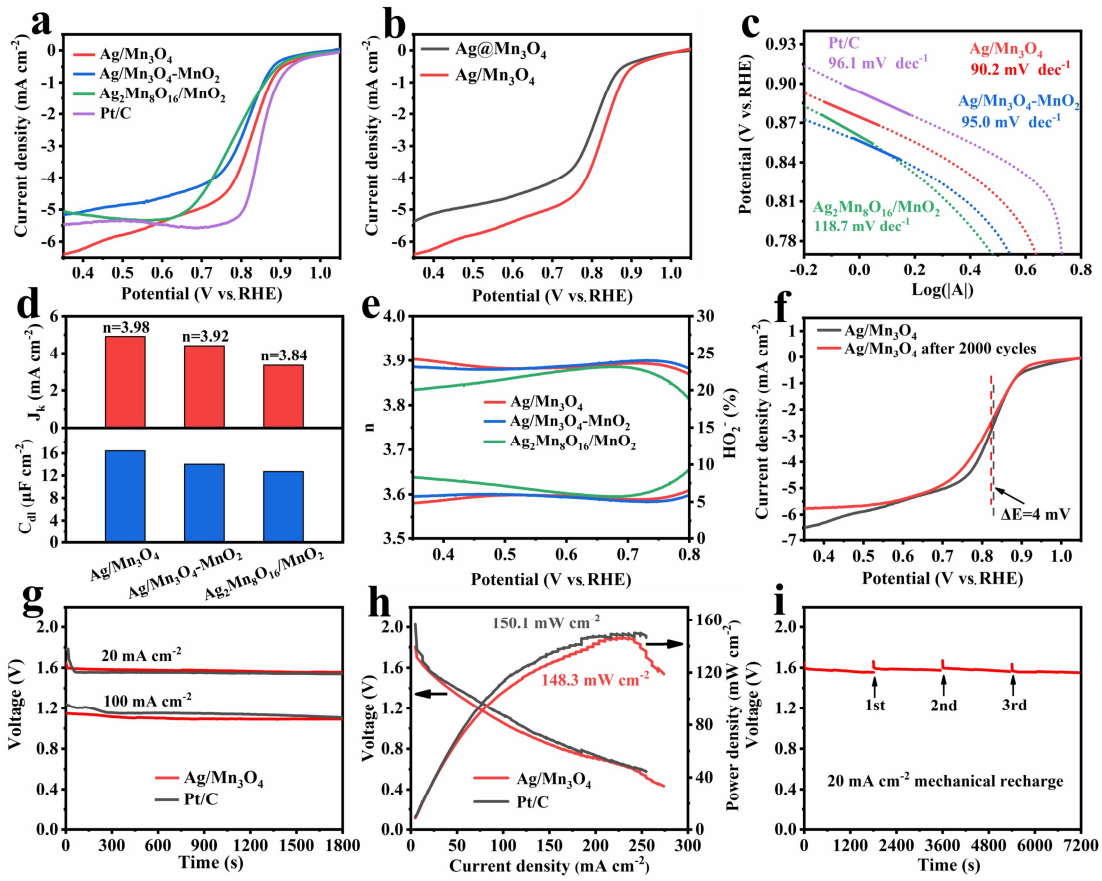

Figure 3 (a) LSV curves of Ag/Mn_3O_4, Ag/Mn_3O_4-MnO_2, and $Ag_2Mn_8O_{16}$/MnO_2. (b)

LSV curves of Ag/Mn_3O_4 and $Ag@Mn_3O_4$ (c) The corresponding Tafel plots. (d) n, $C_{dl,}$ and J_k from the K-L equation. (e) H_2O_2 yields and n from RRDE test of Ag/Mn_3O_4, Ag/Mn_3O_4-MnO_2, and $Ag_2Mn_8O_{16}/MnO_2$ in a 0.1 M KOH alkaline electrolyte. (f) LSV curves before and after 2000 cycles of Ag/Mn_3O_4 in a 0.1 M KOH electrolyte. (g) Galvanostatic discharge curves, (h) current-voltage and power density curves of the Al-air battery with Ag/Mn_3O_4 and Pt/C in a 4 M NaOH electrolyte. (i) Mechanical charging curve of the aqueous alkaline Al-air battery with Ag/Mn_3O_4.

The OER performances of Ag/Mn_3O_4, Ag/Mn_3O_4-MnO_2, and $Ag_2Mn_8O_{16}/MnO_2$ were evaluated in a 1 M KOH electrolyte. The LSV curves of these samples show that Ag/Mn_3O_4 exhibits the lowest OER overpotential (Fig. 4(a)). Fig. 4(b) shows that the Ag/Mn_3O_4 requires only 281 mV and 338 mV to reach the current densities of 5 mA cm^{-2} (η_5) and 10 mA cm^{-2} (η_{10}), indicating the highest OER activity. Meanwhile, the η_{10} of Ag/Mn_3O_4 is lower than those of Ag/Mn_3O_4-1 and Ag/Mn_3O_4-2 (Fig. S24), revealing the Ag/Mn_3O_4 is the optimized sample to achieve highest OER activity. Additionally, the OER electrocatalytic activity of Ag/Mn_3O_4 is also comparable to that of commercial RuO_2 electrocatalyst [44, 45]. Fig. 4(c) displays that the Ag/Mn_3O_4 exhibits the lowest Tafel slope of 77.1 mV dec^{-1} among Ag/Mn_3O_4, Ag/Mn_3O_4-MnO_2, and $Ag_2Mn_8O_{16}/MnO_2$, suggesting the facilitated reaction rate with improved kinetic towards OER. Likewise, the HER performances of these samples were also evaluated. The LSV curves of these samples also manifest that Ag/Mn_3O_4 possesses the lowest HER overpotential (Fig. 4(d)), the Ag/Mn_3O_4 exhibits the lowest η_{10} of 177 mV and

η_{50} of 266 mV, also suggesting the highest HER activity of Ag/Mn_3O_4. Similarly, the η_{10} of Ag/Mn_3O_4 is also lower than those of Ag/Mn_3O_4-1 and Ag/Mn_3O_4-2 (Fig. S25), implying the Ag/Mn_3O_4 is the optimized sample to achieve superior HER activity. Although the overpotential of HER on Ag/Mn_3O_4 is slightly higher than that of commercial Pt/C electrocatalyst, it is still comparable to those of many recently reported advanced HER electrocatalysts (Fig. 4(e)) [46, 47]. The fitted Tafel slopes for HER indicate that the Ag/Mn_3O_4 possesses the lowest Tafel slope of 100.9 mV dec^{-1} among Ag/Mn_3O_4, Ag/Mn_3O_4-MnO_2 and $Ag_2Mn_8O_{16}/MnO_2$ (Fig. 4(f)), also proving boosted HER kinetic with enhanced reaction rate [48]. This optimized reaction kinetic of Ag/Mn_3O_4 might be associated with the formation of the Mott-Schottky heterointerface [48, 49]. The OER and HER stabilities of Ag/Mn_3O_4 were also measured with a current-time chronoamperometric test (Fig. 4(g)). The current retention of Ag/Mn_3O_4 assessed at a constant potential at -0.17 and 1.55 V for 40000 s is 89.7% and 79.4%, respectively, indicating its superior stability for OER and HER. Furthermore, the morphological and chemical states of Ag/Mn_3O_4 after OER and HER testing were also characterized. The TEM images display that the Ag/Mn_3O_4 can still retain its original morphology with nanorod-like shape and Mott-Schottky heterointerface after OER or HER chronoamperometric testing (Fig. S26 and S27). Moreover, the chemical states of Mn and Ag in Ag/Mn_3O_4 after OER or HER testing were revealed by XPS. The doublet of Ag/Mn_3O_4 after OER or HER at 368.2 eV and 374.2 eV in Ag 3d spectra suggests that the chemical state of metallic Ag phase can remain stable (Fig. S28). The Mn 2p spectra of Ag/Mn_3O_4 after OER or

HER display that the Mn^{III}/Mn^{II} intensity ratio increases from 1.44 to 2.03 after OER and from 1.44 to 1.71 after HER (Fig. S29). These results suggest that the main degradation of this Ag/Mn_3O_4 electrocatalyst is the oxidation of Mn_3O_4 phase. Given the best OER and HER performance, the overall water splitting behavior of Ag/Mn_3O_4 and $Ag_2Mn_8O_{16}/MnO_2$ were measured. The LSV curves in Fig. 4(h) show that the Ag/Mn_3O_4 can offer a current density of 10 mA cm^{-2} at 1.71 V, which is lower than that of $Ag_2Mn_8O_{16}/MnO_2$ at 1.89 V. The volume-time curves demonstrate that the volume of collected H_2 and O_2 through the drainage method for Ag/Mn_3O_4 is nearly 2:1, and the Faradic efficiencies are nearly 100% toward overall water splitting (Fig. S30). Moreover, the current retention after overall water splitting at 1.71 V for 60000 s is 82.8% (Fig. 4(i)). All these results confirm the great potential of Ag/Mn_3O_4 for water splitting in practical application.

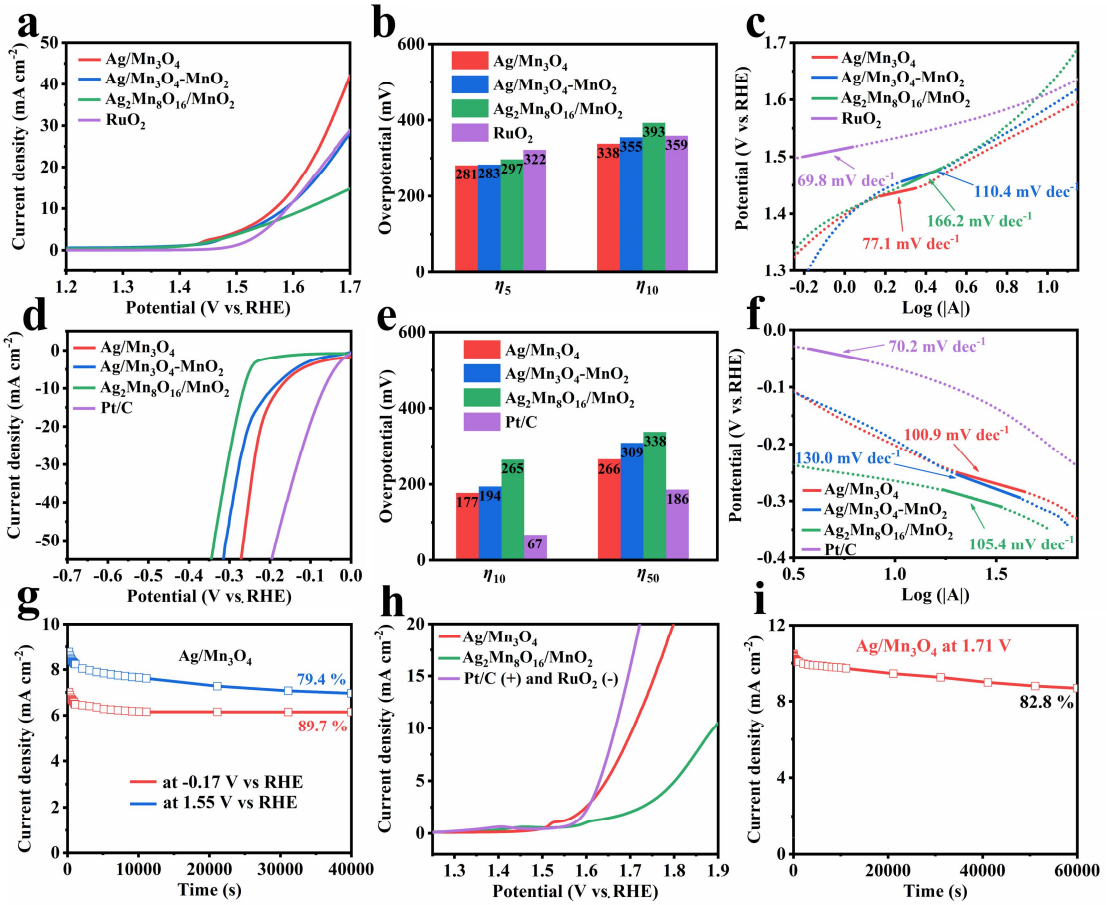

Figure 4 (a) LSV curves, (b) calculated η_5 and η_{10}, and (c) fitted Tafel slopes of Ag/Mn_3O_4, Ag/Mn_3O_4-MnO_2 and $Ag_2Mn_8O_{16}/MnO_2$ for OER. (d) LSV curves, (e) calculated η_{10} and η_{50}, and (f) fitted Tafel slopes of Ag/Mn_3O_4, Ag/Mn_3O_4-MnO_2, and $Ag_2Mn_8O_{16}/MnO_2$ for HER. (g) Current-time chronoamperometric curves of Ag/Mn_3O_4. (h) LSV curves of the electrolytic cell by using Ag/Mn_3O_4 and $Ag_2Mn_8O_{16}/MnO_2$ as both anode and cathode. (i) Corresponding chronoamperometric stability test of Ag/Mn_3O_4 at 1.71 V measured in the electrolytic cell.

To illustrate the catalytic mechanism of Ag/Mn_3O_4 with Mott-Schottky heterointerface towards ORR, OER, and HER, in-situ electrochemical Raman spectroscopy measurement was applied with a series of potential ranges on a

home-made electrochemical cell (Fig. S31). Raman spectra of Ag/Mn_3O_4 at different potentials ranging from 1.01 to 0.41 V (vs. RHE) are shown in Fig. 5(a) to reveal the catalytic mechanism towards ORR. At the beginning, two peaks appeared after an initial open circuit potential was applied. The peak at 654 cm^{-1} can be designated the Mn-O vibration mode in Mn_3O_4 [50], and the other peak at 582 cm^{-1} can be designated to Ag-OH peak resulted from the absorption of OH and oxygen species on the surface of the Ag phase to form Ag-OH^- before ORR [51]. Then, when the external potential negatively shifted to 0.91 V, another new peak (Ag-O) appeared at 622 cm^{-1}. This Ag-O peak can be attributed to the transformation of Ag-OH^- to Ag-O-O^{2-} after interacting with oxygen molecules [52, 53]. Subsequently, when the external potential reached 0.81 V, the Ag-O peak disappeared but the Ag-OH peak remained. This is because the Ag-O-O^{2-} species converted to Ag-O-OH followed by splitting O-O bonds in Ag-O-OH and being transformed into Ag-O^{2-} species which further reacted with H_2O to generate Ag-OH^- [54, 55]. ORR on the Ag phase of Ag/Mn_3O_4 with Mott-Schottky heterointerface is depicted in Fig. 5(b), all oxygen intermediate species preferred to be adsorbed on the Ag phase for reduction. In addition, it is worth noticing that when the conducted external potential is below 0.81 V, the peak intensity of Mn-O began to increase. This is because ORR on the Mn_3O_4 phase can also be activated under this potential and oxygen intermediates began to accumulate on its surface. The whole ORR progress on Ag/Mn_3O_4 can be directed by calculating the peak intensity ratio of Ag-OH to Mn-O ($I_{Ag\text{-}OH}/I_{Mn\text{-}O}$) under different external potentials (Fig. 5(c)). It can be observed that the $I_{Ag\text{-}OH}/I_{Mn\text{-}O}$ increases and then

decreases with the negative shift of the external potential, suggesting that the ORR on Ag occurs in priority to that on Mn_3O_4.

In-situ Raman spectra of Ag/Mn_3O_4 collected under the external potentials range from 1.25 to 1.65 V can be used to analyze the catalytic mechanism towards OER (Fig. 5(d)). When the external potential was 1.25 V, peak at 582 cm^{-1} (Ag-OH) disappeared and peak at 622 cm^{-1} (Ag-O) appeared. This is because under this external potential, the Ag phase on the surface in Ag/Mn_3O_4 was oxidized by the electrochemical perturbation and absorbed water was consumed [56]. Then, with the positive shift of external potential to 1.55 V, the ratio of the peak intensity of Ag-O to that of Mn-O ($I_{Ag\text{-}O}/I_{Mn\text{-}O}$) in Fig. 5(d) began to decrease (Fig. 5(e)), indicating that after OER was activated, oxygen intermediates were absorbed mainly on the surface of Mn_3O_4 phase to intensify the Mn-O peak, suggesting that during OER, Mn_3O_4 phase is more favorable for oxygen intermediate absorption and subsequent oxygen evolution. Moreover, in-situ Raman spectra of Ag/Mn_3O_4 range from -0.1 to -0.5 V can reflect the catalytic mechanism towards HER (Fig. 5(f)). When the external potential is -0.1 V, a peak at 1065 cm^{-1} appeared, which can be assigned to the Ag-H bond [57]. As the external potential negatively shifts to -0.2 V, another new peak at 848 cm^{-1} assigned to the Mn-H bond appeared [58]. Then, these two peaks intensify with the negative shift of external potential. This result also manifests that compared with the Mn_3O_4 phase, the Ag phase is more favorable for the dissociation of water molecules to form adsorb hydrogen during HER.

Based on the observation and discussion above, it can be inferred that the Ag

phase is more favorable for ORR and HER, while the Mn_3O_4 phase is more favorable for OER in Ag/Mn_3O_4. This phenomenon may be attributed to the redistribution of the electronic structure at the Ag/Mn_3O_4 Mott-Schottky heterointerface. Due to the Mott-Schottky effect, electrons flow from the Ag phase to the Mn_3O_4 phase after the formation of the Ag/Mn_3O_4 Mott-Schottky heterointerface to overcome the Mott-Schottky barrier. During this process, metallic Ag is the electron donor and Mn_3O_4 is the electron acceptor [4], and this electron donor-acceptor pair is the key factor resulting in the different roles of active phases in Ag/Mn_3O_4 towards different catalytic reactions. The Ag donor can release electrons, which is favorable for the electrocatalytic reactions consuming electrons including ORR and HER. While the Mn_3O_4 acceptor can accept electrons from adjacent structures, which is beneficial for electrocatalytic oxidation reactions such as OER.

In order to provide an in-depth understanding of the high electrocatalytic activity of Ag/Mn_3O_4 originated from the Mott-Schottky heterointerface with massive electron donor-acceptor pairs, synchrotron radiation spectroscopic characterizations at the atomic level were conducted. The Mn K edge X-ray absorption near-edge structure (XANES) spectra exhibit that the white line of Mn_3O_4 increases accompanied by a negative shift after forming Mott-Schottky heterointerface with Ag (Fig. 5(g)), indicating the increase of electron vacant states and decrease of the average oxidation states of Mn on the Mn_3O_4 phase created by the Ag/Mn_3O_4 Mott-Schottky heterointerface [59]. The Mn-O bond length in Ag/Mn_3O_4 is observed to be 1.39 Å in the Mn K edge extended X-ray absorption fine structure (EXAFS) spectra (Fig.

5(h)), which is longer than its equivalent bond length in Mn_3O_4 of 1.33 Å but much shorter than the Mn-Mn bond length in Mn foil of 2.35 Å. The Wavelet transform (WT) contour plots of Mn foil, Mn_3O_4, and Ag/Mn_3O_4 in Fig. 5(i-k) again confirm the fact that Mn-O is the predominant chemical bond in Ag/Mn_3O_4 rather than Mn-Mn. Furthermore, positions of the intensity maximum in Ag/Mn_3O_4 (5.40 $Å^{-1}$) and Mn_3O_4 (6.20 $Å^{-1}$) are also different, implying the change of Mn coordination environment after forming the Ag/Mn_3O_4 heterointerface [60], corresponding to the fitted results above. Fitting of the EXAFS spectrum of Ag/Mn_3O_4 was conducted to illustrate its structural parameters (Fig. 5(l), Fig. S32, and Table S3), the fitted coordination number of Mn in Ag/Mn_3O_4 is 5.79, which is lower than that in Mn_3O_4 of 5.98 with near-perfect six-coordinated structure.

Based on these results, it can be concluded that at the Ag/Mn_3O_4 heterointerface, Ag atoms with larger atom radius were bonded with Mn_3O_4, enhancing the degree of unsaturation of Mn atoms in the Mn_3O_4 phase at the heterointerface further leading to low charge density on Mn atoms, reduced oxidation state of Mn atoms, and elongated Mn-O bonds at the Mn_3O_4 side of Ag/Mn_3O_4 Mott-Schottky heterointerface. These characteristics allow the Mn_3O_4 phase in Ag/Mn_3O_4 to serve as an electron acceptor to accept electrons transfer from the Ag phase [61]. As a result, the Ag phase releases more electrons and these electrons can participate in the reduction process of reactions consuming electrons including ORR and HER [62]. Conversely, the Mn_3O_4 phase at the Mott-Schottky heterointerface can accept more electrons from the oxygen intermediates further facilitate the OER with oxidation progress [63, 64]. The

conclusion of the synchrotron radiation spectroscopic analysis is consistence with the observation and inference in the in-situ electrochemical Raman measurements above, confirming that the catalytic mechanism of the Ag/Mn_3O_4 Mott-Schottky heterointerface is through the interaction between electron donor-acceptor pairs and intermediate species of different reactions.

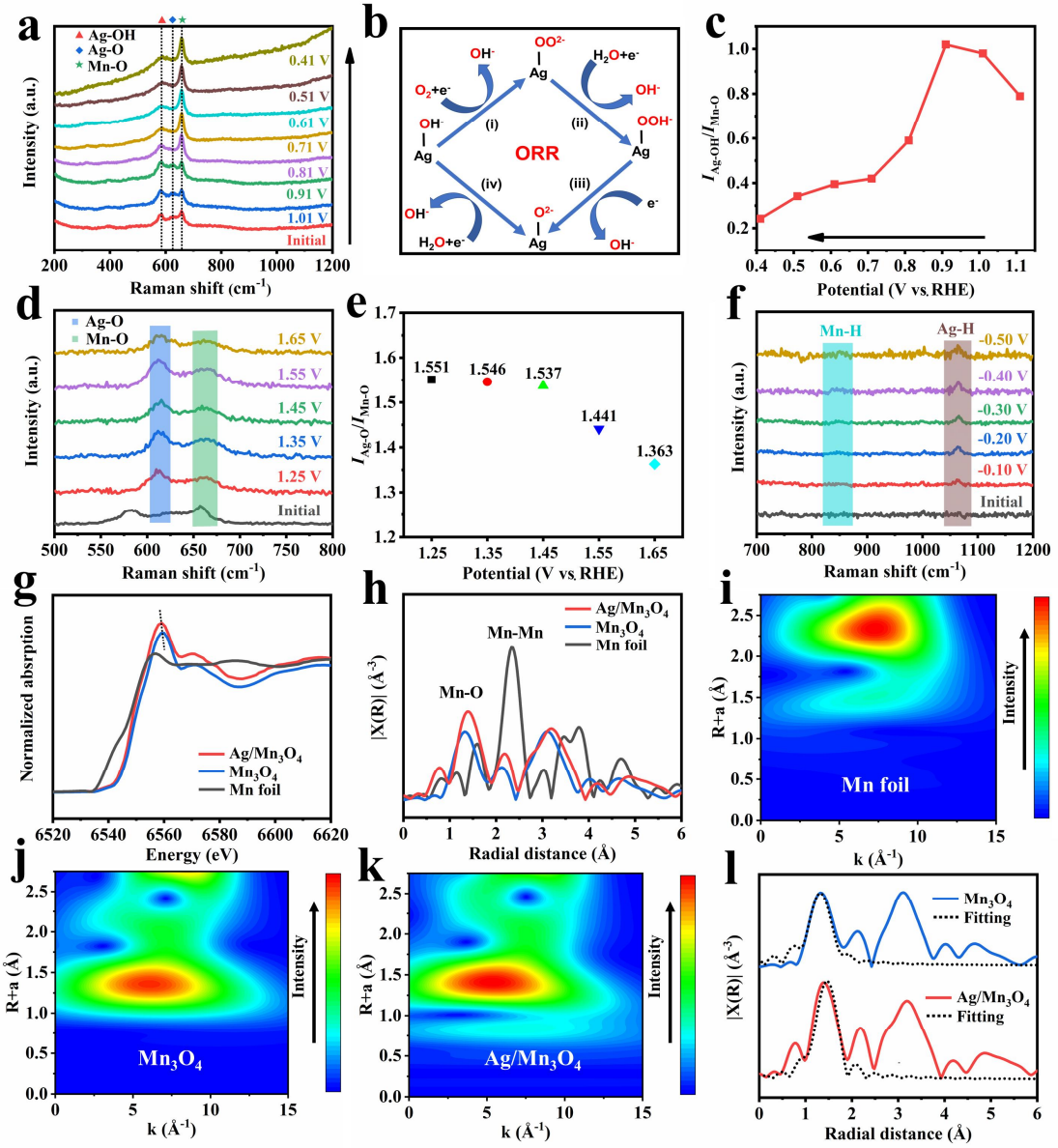

Figure 5 (a) In-situ Raman spectra of Ag/Mn_3O_4 in the range of 1.01 to 0.41 V. (b) Proposed ORR process and (c) intensity ratio of $I_{Ag\text{-}OH}$ to $I_{Mn\text{-}O}$ plot of Ag/Mn_3O_4

under different external potentials in the range of 1.01 to 0.41 V. (d) In-situ Raman spectra range and (e) intensity ratio of $I_{Ag\text{-}O}$ to $I_{Mn\text{-}O}$ plot of Ag/Mn_3O_4 under different external potentials from 1.25 to 1.65 V. (f) In-situ Raman spectra of Ag/Mn_3O_4 from -0.10 V to -0.50 V. Mn K edge (g) XANES and (h) k3-weighted EXAFS spectra of Ag/Mn_3O_4, Mn_3O_4, and Mn foil. (i-k) Wavelet transform (WT) contour plots of (i) Mn foil, (j) Mn_3O_4, and (k) Ag/Mn_3O_4. (l) EXAFS fitting of Ag/Mn_3O_4 and Mn_3O_4 at R space.

3 Conclusions

In summary, the Ag/Mn_3O_4 with Mott-Schottky heterointerface was obtained through the in-situ transformation from $Ag_2Mn_8O_{16}/MnO_2$ with carbon reduction synthesis. The Ag/Mn_3O_4 Mott-Schottky heterointerface with a large Mott-Schottky barrier possesses a more positive valence band and lower band gap than $Ag_2Mn_8O_{16}/MnO_2$ oxide heterointerface, indicating a faster electron transfer pathway causes more electrons involved into catalytic reactions and higher conductivity. Moreover, the Ag/Mn_3O_4 displays a comparable ORR, OER, and HER catalytic performance to noble-metal benchmarks ($E_{1/2}$ = 0.831 V for ORR, η_{10} = 338 mV for OER and η_{10} = 177 mV for HER), which can be mainly attributed to the increase of electron transfer efficiency brought by the formation of Ag/Mn_3O_4 Mott-Schottky heterointerface. Additionally, the assembled alkaline Al-air battery based on Ag/Mn_3O_4 exhibits Pt/C comparable maximum power density of 148.3 mW cm^{-2} and great stability, and the laboratorial water splitting electrolytic cell with Ag/Mn_3O_4

anode and cathode needs low external potential at 1.71 V to achieve the current density of 10 mA cm^{-2} and shows stable long-term discharging plateau, suggesting great potential of Ag/Mn_3O_4 for further practical application in metal-air batteries and hydrogen production. By using synchrotron radiation spectroscopic characterizations to explain the phenomenon observed in in-situ Raman spectra and introducing the concept of donor-acceptor pair, the catalytic mechanism of the Ag/Mn_3O_4 Mott-Schottky heterointerface towards various electrocatalytic reactions has been successfully deciphered. This work not only deepens the understanding of the Mott-Schottky effect on electrocatalysis and fills in the gap in fundamental physical principles that are behind measured electrocatalytic activity but also provides a non-PGM efficient multi-functional electrocatalyst for pushing forward the development of green energy-converting devices.

Conflict and Interest

The authors declare no competing financial interest.

Acknowledgements

This work is financially supported by the National Natural Science Foundation of China (No. 52274302) and Natural Science Foundation of Shanghai (No. 21ZR1429400, 22ZR1429700).

References

[1] Jiang, H.; Sun, Y.; You, B. Dynamic Electrodeposition on Bubbles: An Effective Strategy toward Porous Electrocatalysts for Green Hydrogen Cycling. *Accounts Chem. Res.* **2023**, 10.1021/acs.accounts.3c00059.

[2] Chong, L.; Gao, G.; Wen, J.; Li, H.; Xu, H.; Green, Z.; Sugar, J. D.; Kropf, A. J.; Xu, W.; Lin, X.-M.; Xu, H.; Wang, L.-W.; Liu, D.-J. La- and Mn-doped cobalt spinel oxygen evolution catalyst for proton exchange membrane electrolysis. *Science* **2023,** *380*, 609-616.

[3] Li, H.; Wen, Y.; Jiang, M.; Yao, Y.; Zhou, H.; Huang, Z.; Li, J.; Jiao, S.; Kuang, Y.; Luo, S. Understanding of Neighboring Fe-N_4-C and Co-N_4-C Dual Active Centers for Oxygen Reduction Reaction. *Adv. Funct. Mater.* **2021,** *31*, 2011289.

[4] Li, K.; Cheng, R.; Xue, Q.; Meng, P.; Zhao, T.; Jiang, M.; Guo, M.; Li, H.; Fu, C. In-situ construction of Co/CoSe Schottky heterojunction with interfacial electron redistribution to facilitate oxygen electrocatalysis bifunctionality for zinc-air batteries. *Chem. Eng. J.* **2022,** *450*, 137991.

[5] Sun, F.; Wang, G.; Ding, Y.; Wang, C.; Yuan, B.; Lin, Y. NiFe-Based Metal-Organic Framework Nanosheets Directly Supported on Nickel Foam Acting as Robust Electrodes for Electrochemical Oxygen Evolution Reaction. *Adv. Energy Mater.* **2018,** *8*, 1800584.

[6] Quílez-Bermejo, J.; García-Dalí, S.; Daouli, A.; Zitolo, A.; Canevesi, R. L. S.; Emo, M.; Izquierdo, M. T.; Badawi, M.; Celzard, A.; Fierro, V. Advanced Design of Metal Nanoclusters and Single Atoms Embedded in C1N1-Derived Carbon Materials

for ORR, HER, and OER. *Adv. Funct. Mater.* **2023,** *33*, 2300405.

[7] Cheng, R.; Li, K.; Li, Z.; Jiang, M.; Wang, F.; Yang, Z.; Zhao, T.; Meng, P.; Fu, C. Rational design of boron-nitrogen coordinated active sites towards oxygen reduction reaction in aluminum-air batteries with robust integrated air cathode. *J. Power Sources* **2023,** *556*, 232476.

[8] Li, Z.; Zhang, Y.; Feng, Y.; Cheng, C.-Q.; Qiu, K.-W.; Dong, C.-K.; Liu, H.; Du, X.-W. Co_3O_4 Nanoparticles with Ultrasmall Size and Abundant Oxygen Vacancies for Boosting Oxygen Involved Reactions. *Adv. Funct. Mater.* **2019,** *29*, 1903444.

[9] Li, Y.; Talib, S. H.; Liu, D.; Zong, K.; Saad, A.; Song, Z.; Zhao, J.; Liu, W.; Liu, F.; Ji, Q.; Tsiakaras, P.; Cai, X. Improved oxygen evolution reaction performance in $Co_{0.4}Mn_{0.6}O_2$ nanosheets through Triple-doping (Cu, P, N) strategy and its application to Zn-air battery. *Appl. Catal. B Environ.* **2023,** *320*, 122023.

[10] Zhu, J.; Xiao, M.; Li, G.; Li, S.; Zhang, J.; Liu, G.; Ma, L.; Wu, T.; Lu, J.; Yu, A.; Su, D.; Jin, H.; Wang, S.; Chen, Z. A Triphasic Bifunctional Oxygen Electrocatalyst with Tunable and Synergetic Interfacial Structure for Rechargeable Zn-Air Batteries. *Adv. Energy Mater.* **2020,** *10*, 1903003.

[11] Li, K.; Wang, C.; Li, H.; Wen, Y.; Wang, F.; Xue, Q.; Huang, Z.; Fu, C. Heterostructural Interface in Fe_3C-TiN Quantum Dots Boosts Oxygen Reduction Reaction for Al-Air Batteries. *ACS Appl. Mater. Interfaces* **2021,** *13*, 47440-47448.

[12] Albu, Z.; Alzaid, F.; AlQahtani, S.; Abass, N. A.; Alenazey, F.; Allehyani, I.; AlOtaibi, B. Improving water oxidation performance by implementing heterointerfaces between ceria and metal-oxide nanoparticles. *J. Colloid and Interface*

Sci. **2021,** *587*, 39-46.

[13] Jiang, L.; Zhang, Y.-J.; Luo, X.-H.; Yu, L.; Li, H.-X.; Li, Y.-J. Se and O co-insertion induce the transition of MoS_2 from 2H to 1T phase for designing high-active electrocatalyst of hydrogen evolution reaction. *Chem. Eng. J.* **2021,** *425*, 130611.

[14] Zhang, L.; Lei, Y.; Xu, W.; Wang, D.; Zhao, Y.; Chen, W.; Xiang, X.; Pang, X.; Zhang, B.; Shang, H. Highly active and durable nitrogen-doped CoP/CeO_2 nanowire heterostructures for overall water splitting. *Chem. Eng. J.* **2023,** *460*, 141119.

[15] Yang, X.; Zheng, X.; Li, H.; Luo, B.; He, Y.; Yao, Y.; Zhou, H.; Yan, Z.; Kuang, Y.;Huang, Z. Non-Noble-Metal Catalyst and Zn/Graphene Film for Low-Cost and Ultra-Long-Durability Solid-State Zn-Air Batteries in Harsh Electrolytes. *Adv. Funct. Mater.* **2022,** *32*, 2200397.

[16] Kaltak, M.; Fernández-Serra, M.; Hybertsen, M. S. Charge localization and ordering in $A_2Mn_8O_{16}$ hollandite group oxides: Impact of density functional theory approaches. *Phys. Rev. Mater.* **2017,** *1* (7), 075401.

[17] Zhou, Y.; Chu, B.; Sun, Z.; Dong, L.; Wang, F.; Li, B.; Fan, M.; Chen, Z. Surface reconstruction and charge distribution enabling Ni/W_5N_4 Mott-Schottky heterojunction bifunctional electrocatalyst for efficient urea-assisted water electrolysis at a large current density. *Appl. Catal. B Environ.* **2023,** *323*, 122168.

[18] Wang, X.; Li, M.; Wang, P.; Sun, D.; Ding, L.; Li, H.; Tang, Y.; Fu, G. Spin-Selective Coupling in Mott-Schottky Er_2O_3-Co Boosts Electrocatalytic Oxygen Reduction. *Small Methods* **2023,** 10.1002/smtd.202300100.

[19] Chen, T.; Guo, S.; Yang, J.; Xu, Y.; Sun, J.; Wei, D.; Chen, Z.; Zhao, B.; Ding, W. Nitrogen-Doped Carbon Activated in Situ by Embedded Nickel through the Mott-Schottky Effect for the Oxygen Reduction Reaction. *ChemPhysChem* **2017,** *18*, 3454-3461.

[20] Yao, Y.; Wu, J.; Feng, Q.; Zeng, K.; Wan, J.; Zhang, J.; Mao, B.; Hu, K.; Chen, L.; Zhang, H.; Gong, Y.; Yang, K.; Zhou, H.; Huang, Z.; Li, H. Spontaneous Internal Electric Field in Heterojunction Boosts Bifunctional Oxygen Electrocatalysts for Zinc-Air Batteries: Theory, Experiment, and Application. *Small* **2023,** 10.1002/smll.202302015.

[21] Su, H.; Zhang, K.-X.; Zhang, B.; Wang, H.-H.; Yu, Q.-Y.; Li, X.-H.; Antonietti, M.; Chen, J.-S. Activating Cobalt Nanoparticles via the Mott–Schottky Effect in Nitrogen-Rich Carbon Shells for Base-Free Aerobic Oxidation of Alcohols to Esters. *J. Am. Chem. Soc.* **2017,** *139*, 811-818.

[22] Yang, H.; Wang, B.; Kou, S.; Lu, G.; Liu, Z. Mott-Schottky heterojunction of Co/Co_2P with built-in electric fields for bifunctional oxygen electrocatalysis and zinc-air battery. *Chem. Eng. J.* **2021,** *425*, 131589.

[23] Sun, Z.; Wang, Y.; Zhang, L.; Wu, H.; Jin, Y.; Li, Y.; Shi, Y.; Zhu, T.; Mao, H.; Liu, J.; Xiao, C.; Ding, S. Simultaneously Realizing Rapid Electron Transfer and Mass Transport in Jellyfish-Like Mott-Schottky Nanoreactors for Oxygen Reduction Reaction. *Adv. Funct. Mater.* **2020,** *30*, 1910482.

[24] Li, G.; Jiang, M.; Liao, Q.; Ding, R.; Gao, Y.; Jiang, L.; Zhang, D.; Chen, S.; He, H. Directly anchoring Ag single atoms on α-MnO_2 nanorods as efficient oxygen

reduction catalysts for Mg-air fuel cell. *J. Alloys Compd.* **2021,** *858*, 157672.

[25] Wang, J.; Xie, H.; Shu, D.; Chen, T.; Liu, H.; Zou, X.; Chen, D. The promotion of NH_3-SCR performance and its mechanism on Sm modified birnessite. *Fuel* **2024,** *356*, 129604.

[26] Wu, S.; Liu, H.; Huang, Z.; Xu, H.; Shen, W. O-vacancy-rich porous MnO_2 nanosheets as highly efficient catalysts for propane catalytic oxidation. *Appl. Catal. B Environ.* **2022,** *312*, 121387.

[27] Li, T.; Hu, Y.; Liu, K.; Yin, J.; Li, Y.; Fu, G.; Zhang, Y.; Tang, Y. Hollow yolk-shell nanoboxes assembled by Fe-doped Mn_3O_4 nanosheets for high-efficiency electrocatalytic oxygen reduction in Zn-Air battery. *Chem. Eng. J.* **2022,** *427*, 131992.

[28] Liu, K.; Huang, X.; Wang, H.; Li, F.; Tang, Y.; Li, J.; Shao, M. Co_3O_4-CeO_2/C as a Highly Active Electrocatalyst for Oxygen Reduction Reaction in Al-Air Batteries. *ACS Appl. Mater. Interfaces* **2016,** *8*, 34422-34430.

[29] Liang, S.; Teng, F.; Bulgan, G.; Zong, R.; Zhu, Y. Effect of Phase Structure of MnO_2 Nanorod Catalyst on the Activity for CO Oxidation. *J. Phys. Chem. C* **2008,** *112*, 5307-5315.

[30] Jia, J.; Zhang, P.; Chen, L. Catalytic decomposition of gaseous ozone over manganese dioxides with different crystal structures. *Appl. Catal. B Environ.* **2016,** *189*, 210-218.

[31] Sharma, R.; Dar, S. A.; Mishra, A. K. Structure, electronic, magnetic and optical properties of cubic $Hf_{1-x}(TM)_xO_2$ (X = 0, 0.25, TM = Mn, Fe, Co, Ni): A first principle investigation. *J. Alloys Compd.* **2019,** *791*, 983-993.

[32] Deng, D.; Yu, L.; Chen, X.; Wang, G.; Jin, L.; Pan, X.; Deng, J.; Sun, G.; Bao, X. Iron Encapsulated within Pod-like Carbon Nanotubes for Oxygen Reduction Reaction. *Angew. Chem. Int. Ed.* **2013,** *52*, 371-375.

[33] Xue, Z.-H.; Han, J.-T.; Feng, W.-J.; Yu, Q.-Y.; Li, X.-H.; Antonietti, M.; Chen, J.-S. Tuning the Adsorption Energy of Methanol Molecules Along Ni-N-Doped Carbon Phase Boundaries by the Mott–Schottky Effect for Gas-Phase Methanol Dehydrogenation. *Angew. Chem. Int. Ed.* **2018,** *57*, 2697-2701.

[34] Li, X.; Pan, Y.; Yi, H.; Hu, J.; Yang, D.; Lv, F.; Li, W.; Zhou, J.; Wu, X.; Lei, A.; Zhang, L. Mott-Schottky Effect Leads to Alkyne Semihydrogenation over Pd-Nanocube@N-Doped Carbon. *ACS Catal.* **2019,** *9*, 4632-4641.

[35] Zou, X.; Dong, Y.; Ke, J.; Ge, H.; Chen, D.; Sun, H.; Cui, Y. Cobalt monoxide/tungsten trioxide p-n heterojunction boosting charge separation for efficient visible-light-driven gaseous toluene degradation. *Chem. Eng. J.* **2020,** *400*, 125919.

[36] Gu, W.; Song, Y.; Liu, J.; Wang, F. Lanthanum-Based Compounds: Electronic Band-Gap-Dependent Electrocatalytic Materials for Oxygen Reduction Reaction. *Chem. Eur. J.* **2017,** *23*, 10126-10132.

[37] Li, K.; Cheng, R.; Xue, Q.; Zhao, T.; Wang, F.; Fu, C. Construction of a Co/MnO Mott-Schottky Heterostructure to Achieve Interfacial Synergy in the Oxygen Reduction Reaction for Aluminum-Air Batteries. *ACS Appl. Mater. Interfaces* **2023,** *15*, 9150-9159.

[38] Bolar, S.; Shit, S.; Murmu, N. C.; Samanta, P.; Kuila, T. Activation Strategy of MoS_2 as HER Electrocatalyst through Doping-Induced Lattice Strain, Band Gap

Engineering, and Active Crystal Plane Design. *ACS Appl. Mater. Interfaces* **2021,** *13*, 765-780.

[39] Ji, B.; Gou, J.; Zheng, Y.; Pu, X.; Wang, Y.; Kidkhunthod, P.; Tang, Y. Coordination Chemistry of Large-Sized Yttrium Single-Atom Catalysts for Oxygen Reduction Reaction. *Adv. Mater.* **2023,** *35*, 2300381.

[40] Wu, L.; Li, S.; Li, L.; Zhang, H.; Tao, L.; Geng, X.; Yang, H.; Zhou, W.; Sun, C.; Ju, D.; An, B. Modest modulation on the electronic structure of Co_9S_8 by vanadium doping for high-performance rechargeable Zn-air batteries. *Appl. Catal. B Environ.* **2023,** *324*, 122250.

[41] Kim, H. W.; Bukas, V. J.; Park, H.; Park, S.; Diederichsen, K. M.; Lim, J.; Cho, Y. H.; Kim, J.; Kim, W.; Han, T. H.; Voss, J.; Luntz, A. C.; McCloskey, B. D. Mechanisms of Two-Electron and Four-Electron Electrochemical Oxygen Reduction Reactions at Nitrogen-Doped Reduced Graphene Oxide. *ACS Catal.* **2020,** *10*, 852-863.

[42] Yu, F.; Zhan, J.; Chen, D.; Guo, J.; Zhang, S.; Zhang, L.-H. Electronic States Regulation Induced by the Synergistic Effect of Cu Clusters and Cu-S_1N_3 Sites Boosting Electrocatalytic Performance. *Adv. Funct. Mater.* **2023,** *33*, 2214425.

[43] Li, X.; Wu, X.; Zhao, Y.; Lin, Y.; Zhao, J.; Wu, C.; Liu, H.; Shan, L.; Yang, L.; Song, L.; Jiang, J. Promoting Oxygen Reduction Reaction by Inducing Out-of-Plane Polarization in a Metal Phthalocyanine Catalyst. *Adv. Mater.* **2023,** 10.1002/adma.202302467.

[44] Yasin, G.; Ali, S.; Ibraheem, S.; Kumar, A.; Tabish, M.; Mushtaq, M. A.; Ajmal,

S.; Arif, M.; Khan, M. A.; Saad, A.; Qiao, L.; Zhao, W. Simultaneously Engineering the Synergistic-Effects and Coordination-Environment of Dual-Single-Atomic Iron/Cobalt-sites as a Bifunctional Oxygen Electrocatalyst for Rechargeable Zinc-Air Batteries. *ACS Catal.* **2023,** *13*, 2313-2325.

[45] Wang, H.; Sun, C.; Zhu, E.; Shi, C.; Yu, J.; Xu, M. Core-shell MOF-derived Fe_3C-Co-NC as high-performance ORR/OER bifunctional catalyst. *J. Alloys Compd.* **2023,** *948*, 169728.

[46] Cho, S.; Yim, G.; Koh, J.; Jang, H.; Park, J. T. One-pot synthesis of Pt@TiO_2 core-shell nanoparticles for stable hydrogen evolution reaction in acidic and alkaline media. *Mater. Today Chem.* **2023,** *32*, 101644.

[47] Zhang, Y.; Chen, S.; Zhang, Y.; Li, R.; Zhao, B.; Peng, T. Hydrogen-Bond Regulation of the Microenvironment of Ni(II)-Porphyrin Bifunctional Electrocatalysts for Efficient Overall Water Splitting. *Adv. Mater.* **2023,** *35*, 2210727.

[48] Cai, W.; Zhou, C.; Hu, X.; Jiao, T.; Liu, Y.; Li, L.; Li, J.; Kitano, M.; Hosono, H.; Wu, J. Quasi-Two-Dimensional Intermetallic Electride CeRuSi for Efficient Alkaline Hydrogen Evolution. *ACS Catal.* **2023,** *13*, 4752-4759.

[49] Wang, S.; Xu, B.; Huo, W.; Feng, H.; Zhou, X.; Fang, F.; Xie, Z.; Shang, J. K.; Jiang, J. Efficient FeCoNiCuPd thin-film electrocatalyst for alkaline oxygen and hydrogen evolution reactions. *Appl. Catal. B Environ.* **2022,** *313*, 121472.

[50] Yang, L. W.; Wu, X. L.; Huang, G. S.; Qiu, T.; Yang, Y. M. In situ synthesis of Mn-doped ZnO multileg nanostructures and Mn-related Raman vibration. *J. Appl. Phys.* **2004,** *97*, 014308.

[51] Savinova, E. R.; Kraft, P.; Pettinger, B.; Doblhofer, K. In situ Raman spectroscopy studies of the interface between silver (111) electrodes and alkaline NaF electrolytes. *J. Electroanal. Chem.* **1997,** *430*, 47-56.

[52] Waterhouse, G. I. N.; Bowmaker, G. A.; Metson, J. B. Oxygen chemisorption on an electrolytic silver catalyst: a combined TPD and Raman spectroscopic study. *Appl. Surf. Sci.* **2003,** *214*, 36-51.

[53] Ren, L.; Dai, W.; Yang, X.; Cao, Y.; Xie, Z.; Fan, K. Transformation of Various Oxygen Species on the Surface of Electrolytic Silver Characterized by in Situ Raman Spectroscopy. *Chinese J. Catal.* **2006,** *27*, 115-118.

[54] Zhong, H.; Ly, K. H.; Wang, M.; Krupskaya, Y.; Han, X.; Zhang, J.; Zhang, J.; Kataev, V.; Buchner, B.; Weidinger, I. M.; Kaskel, S.; Liu, P.; Chen, M.; Dong, R.; Feng, X. A Phthalocyanine-Based Layered Two-Dimensional Conjugated Metal-Organic Framework as a Highly Efficient Electrocatalyst for the Oxygen Reduction Reaction. *Angew. Chem. Int. Ed.* **2019,** *58*, 10677-10682.

[55] Dong, J.-C.; Su, M.; Briega-Martos, V.; Li, L.; Le, J.-B.; Radjenovic, P.; Zhou, X.-S.; Feliu, J. M.; Tian, Z.-Q.; Li, J.-F. Direct In Situ Raman Spectroscopic Evidence of Oxygen Reduction Reaction Intermediates at High-Index Pt (hkl) Surfaces. *J. Am. Chem. Soc.* **2020,** *142*, 715-719.

[56] Benedetti, A. V.; Nakazato, R. Z.; Sumodjo, P. T. A.; Cabot, P. L.; Centellas, F. A.; Garrido, J. A. Potentiodynamic behaviour of Cu-A1-Ag alloys in NaOH: a comparative study related to the pure metals electrochemistry. *Electrochim. Acta* **1991,** *36*, 1409-1421.

[57] Yang, Y.; Wang, Y.; Zhang, X.; Qi, G.; Xu, S.; Xu, W. A facile method of removing several common surface-enhanced Raman scattering probe molecules adsorbed on Ag with sodium borohydride solution. *J. Optics* **2015,** *17*, 075003.

[58] Koleva, V.; Stefov, V.; Cahil, A.; Najdoski, M.; Šoptrajanov, B.; Engelen, B.; Lutz, H. D. Infrared and Raman studies of manganese dihydrogen phosphate dihydrate, $Mn(H_2PO_4)_2 \cdot 2H_2O$. I: Region of the vibrations of the phosphate ions and external modes of the water molecules. *J. Mol. Struct.* **2009,** *917*, 117-124.

[59] Su, H.; Zhou, W.; Zhou, W.; Li, Y.; Zheng, L.; Zhang, H.; Liu, M.; Zhang, X.; Sun, X.; Xu, Y.; Hu, F.; Zhang, J.; Hu, T.; Liu, Q.; Wei, S. In-situ spectroscopic observation of dynamic-coupling oxygen on atomically dispersed iridium electrocatalyst for acidic water oxidation. *Nature Commun.* **2021,** *12*, 6118.

[60] Yu, P.; Wang, L.; Sun, F.; Xie, Y.; Liu, X.; Ma, J.; Wang, X.; Tian, C.; Li, J.; Fu, H. Co Nanoislands Rooted on Co-N-C Nanosheets as Efficient Oxygen Electrocatalyst for Zn-Air Batteries. *Adv. Mater.* **2019,** *31*, 1901666.

[61] Luo, L.; Fu, L.; Liu, H.; Xu, Y.; Xing, J.; Chang, C.-R.; Yang, D.-Y.; Tang, J. Synergy of Pd atoms and oxygen vacancies on In_2O_3 for methane conversion under visible light. *Nature Commun.* **2022,** *13*, 2930.

[62] Talukder, N.; Wang, Y.; Nunna, B. B.; Lee, E. S. Nitrogen-doped graphene nanomaterials for electrochemical catalysis/reactions: A review on chemical structures and stability. *Carbon* **2021,** *185*, 198-214.

[63] Ni, S.; Qu, H.; Xing, H.; Xu, Z.; Zhu, X.; Yuan, M.; Wang, L.; Yu, J.; Li, Y.; Yang, L.; Liu, H., Donor-Acceptor Couples of Metal and Metal Oxides with Enriched Ni^{3+}

Active Sites for Oxygen Evolution. *ACS Appl. Mater. Interfaces* **2021,** *13*, 17501-17510.

[64] Yang, M.; Zhang, Y.; Jian, J.; Fang, L.; Li, J.; Fang, Z.; Yuan, Z.; Dai, L.; Chen, X.; Yu, D. Donor-Acceptor Nanocarbon Ensembles to Boost Metal-Free All-pH Hydrogen Evolution Catalysis by Combined Surface and Dual Electronic Modulation. *Angew. Chem. Int. Ed.* **2019,** *58*, 16217-16222.